scientific reports

Check for updates

OPEN

Effects of triaxial rolling on the microstructure and installation characteristics of reactor pressure vessel studs

Wei Zhu[1,2], Hua Li[3], Decheng Wang[1]✉, Peng Cheng[4], Luoxing Li[2], Feng Feng[1] & Peng Zhou[1]

Reactor pressure vessel (RPV) studs are key components of nuclear reactors, and their connection with flange ensures the sealing of the RPV under high-pressure and high-temperature conditions. In the present work, the external threads of the RPV stud were prepared by triaxial rolling, and the texture evolution of the external thread root material of an RPV stud was predicted by finite element analysis coupled with viscoplastic self-consistent simulations. The microstructure of the external thread root material of RPV stud was characterized by scanning electron microscope and electron back-scattered diffraction. The installation characteristics of the turned and rolled parts of the RPV stud were tested by installation and pretightening tests. It was found that the dynamic recrystallization at the external thread root formed ultrafine tempered sorbite grains, high-angle grain boundaries (47%), and strong {111} <110> and {111} <112> textures. In the installation and pretightening test, the residual elongation of rolled parts was reduced by 6% under the same loading pressure. The triaxial rolling process distributed the microstructure of the external thread root of the RPV stud in a gradient manner, resulting in improved stud installation characteristics.

Keywords Reactor pressure vessel stud, Triaxial rolling, Microstructure, Assembly performance

Reactor pressure vessel (RPV) studs are important components of nuclear reactors, which are generally subjected to high temperature, internal pressure, preload, and hydrostatic loading for a long time[1,2]. RPV studs have oversized diameters (nominal diameter is greater than 100 mm), and are therefore currently processed by the traditional turning method. However, turning is prone to accumulative thread errors[3] and inevitably generates defects, such as tool marks and surface tissue damage[4]; thus, it is difficult for RPV studs to meet initial design requirements. The fracture of RPV studs rarely occurs in nuclear reactors, and the most common problems are the deformation and jamming of the external threads of RPV studs during assembly and operation due to insufficient strength and precision[1]. Therefore, to improve the installation characteristics of the RPV studs, this paper utilizes triaxial rolling instead of turning to enhance the installation performance of RPV studs.

In the cold rolling of threads, which began to develop in the 1990s, a thread rolling die is pressed into a workpiece blank to produce plastic deformation and form threads with a mirror of the rolling die, resulting in better thread geometric accuracy and mechanical properties[5–7]. The optimization of cold rolling process parameters for threads, such as blank diameter, friction coefficient, and heat-treatment temperature, has been extensively performed[8,9]. Mohandesi et al.[10] rolled and turned AISI 1035 steel bolts and found that the fatigue strength of the rolled threads increased by 55% as compared to that of the turned bolts. The increase in the dislocation density of the ferritic phase of the rolled threads was the main factor for strengthening. Zhu et al.[11] analyzed thread characteristics under different lubrication and operating conditions of an axial feed thread rolling process and noticed that strong shear stress led to the elongation and refinement of the bottom and lateral grains of the threads, increased the fraction of low-angle grain boundaries, and improved the strength and hardness of the threads. Kao et al.[12] developed an integrated CAD/CAE/CAM system for thread rolling. In this system, a thread rolling mold was first automatically generated in Solidworks software and then imported into deform 3D software to analyze the screw angle, the effective stress, the axial motion, and the radial load. Nitu et al.[13]

[1]China Productivity Center for Machinery, China Academy of Machinery Science and Technology, Beijing 100044, China. [2]College of Mechanical and Vehicle Engineering, Hunan University, Changsha 410082, Hunan, China. [3]China Nuclear Power Engineering Co., Ltd, Beijing 100044, China. [4]Yanqi Lake (Beijing) Institute of Basic Manufacturing Technology Research Co., Ltd, Beijing 100044, China. ✉email: zhudhmiao@gmail.com

established a numerical model of wedge rolling. Zhang et al.[14] developed a three-dimensional (3D) model of thread cold rolling to investigate the forming characteristics of threads and asserted that the axial and radial flow of the metal during thread forming was significant, whereas its circumferential flow was small. Moreover, the equivalent force (strain) in the thread contour region was larger than that in the central region of the workpiece.

The aforesaid experimental investigations have primarily focused on the rolling process and macroscopic performance of small-sized bolts. The numerical simulations mainly concentrate on the macroscopic deformation, stress–strain, and force distribution during the thread rolling process. In order to solve the problem of degradation and failure of RPV stud, many researchers have conducted studies on material selection[15], heat treatment process[16], and bolt preload control[17], which have effectively improved the performance of RPV studs. However, there is little research report on the rolling process and microstructure evolution of the external threads of the RPV studs.

The viscoplastic self-consistent model (VPSC) was proposed by Lebensohn and Tomé[18] and is often adopted to predict the plastic deformation behavior[19,20], and microstructure evolution during rolling[21,22]. Chen et al.[23] established symmetric and asymmetric rolling models based on FEM and VPSC simulations to study the structure and texture evolution of Mg-3Al-1Zn alloy at different temperatures and stress levels and found that shear deformation played a crucial role in the activation of the deformation mode by increasing the effective Schmidt factor to promote twinning and slip. Mishin et al.[24] adopted the VPSC model to predict the crystal texture of beryllium after cold deformation and asserted that the deformation of polycrystalline beryllium during cold rolling occurred by < 11–20 > slip. Saleh et al.[25] applied the VPSC model to predict the texture evolution of Fe-28Mn-0.28C steel with cold rolling thickness reductions of 12–80% and propounded that the texture of Fe-28Mn-0.28C steel consisted of strong α-fibers and weak γ-fibers.

In this study, we will focus on the microstructural evolution of RPV studs and the changes in their installation properties. The external threads of an RPV stud were fabricated by triaxial rolling and the microstructure of the external thread root was characterized in depth. The texture distributions of the surface and subsurface layers of the external thread root of the RPV stud after rolling were predicted by finite element analysis coupled with VPSC simulations, and the simulation results were compared with electron back-scattered diffraction (EBSD) data to verify the accuracy of the VPSC model. A 1:1 installation and pretightening tests were performed on the turned and rolled parts of the RPV stud. It was found that the microstructure of the external thread root material of the rolled RPV stud was distributed in a gradient manner from the surface to the subsurface layers and the surface had a strong rolling texture. Hence, the rolled RPV stud had better installation preload characteristics.

Experiments

Triaxial rolling process

The external threads of the short RPV stud blank were rolled on a triaxial rolling machine (Fig. 1). The material of the rolling die was Cr12MoV. The diameters of the rolling die and the RPV stud blank were 283 mm and 168 mm, respectively. Under hydraulic pressure, three rolling dies were simultaneously fed radially to cold extrude the external surface of the RPV stud, and the RPV stud moved axially following the rotation of the rolling die. The dimensions of the RPV stud are shown in Fig. 2.

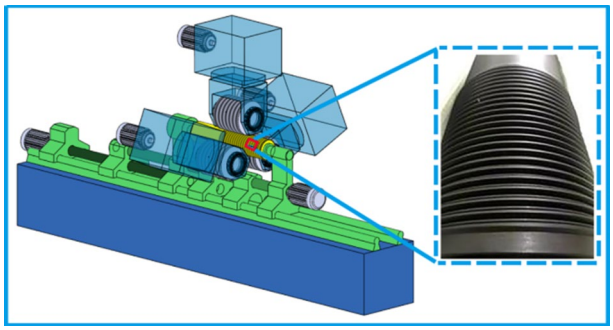

Figure 1. Schematic diagram of the triaxial rolling process and photo of the reactor pressure vessel stud.

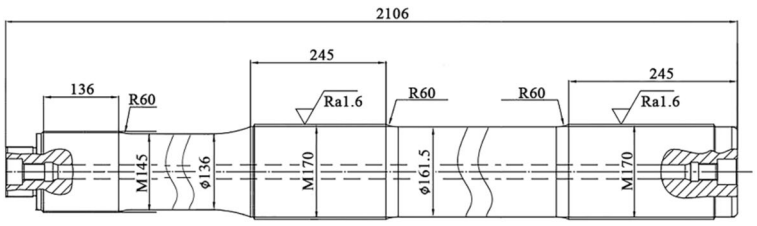

Figure 2. Dimensions of the reactor pressure vessel stud (all units in mm).

Sample preparation and characterization

The experimental material was 40CrNi2MoV steel, and its AFNOR brand was 40NCDV7-03. After forging, the RPV Stud was heat treated by water quenching and oil cooling at 850 °C, then tempered at 620 °C, and finally, oil-cooled after holding for six hours. The chemical composition of 40CrNi2MoV steel was determined by inductively coupled plasma emission spectrometry (ICP) (Table 1).

EBSD samples (S1, S2, S3, S4) were prepared from the root surface, subsurface (surface to surface distance = − 400 μm and − 800 μm), and matrix of the threaded section of the RPV stud (Fig. 3). The polished samples were etched with a 4% nitrite solution. The microstructures of the S1, S2, S3, and S4 samples on the RD-TD and ND-TD planes were observed by EBSD with a step size of 0.075 μm.

Finite element model development

First, hardening deformation parameters were determined by compression tests, and then a simplified finite element 3D model was established to predict the deformation behavior and velocity gradients of the thread rolling process based on VPSC simulations. The VPSC model was used to analyze microstructure distribution and evolution during the thread-rolling process.

The triaxial rolling process of the RPV stud was simulated in ABAQUS software. The macroscopic deformation process of 40CrNi2MoV steel was described by the Johnson–Cook (JC) model[11,26], and the obtained model parameters are shown in Table 2. The deformation gradient was derived using the VUMAT subroutine, as shown in Fig. 6. The three rolling dies were set as discrete rigid bodies to simplify the calculation (Fig. 4a). All three rolling dies have the same structure, with a thread height of 3.4 mm and a thread angle of 60°. They all rotated clockwise at 5 r/min (the center point of their upper surface circle was the reference point; radial feed depth = 2.25 mm). The RPV stud billet was set as a plastic body without considering the Bauschinger effect. The geometric model of the RPV stud billet was simplified to a circle with a radial thickness of 8 mm and a diameter of 168 mm. The inner surface of the circle was constrained by six degrees of freedom to replace the non-deformed middle area of the billet. The mesh size along the radial direction of the rings was set to single accuracy. The mesh size from the outer ring to the inner ring was 0.08, and in the circumferential direction, the mesh sizes of the inner and outer rings were 1.5 and 0.5, respectively. The meshes were performed with 8-node C3D8R elements and controlled by stiffness hourglass. The Arbitrary Lagrangian Eulerian adaptive mesh was used to ensure the mesh quality under large deformations. A circular compression test[27] was used to determine the friction coefficient (μ = 0.2). The metallographic morphology of the thread cross-section is compared with the stress distribution simulation, and it can be seen from the metallographic map (Fig. 4b) that there are obvious metal flow lines in the root of the thread, which are getting thinner and thinner from the surface layer towards the core

C	Si	Mn	Cr	Ni	Cu	Mo	V	Fe
40	0.22	0.76	0.81	1.76	0.012	0.45	0.042	Balance

Table 1. Chemical composition of 40CrNi2MoV7-03 steel (wt%).

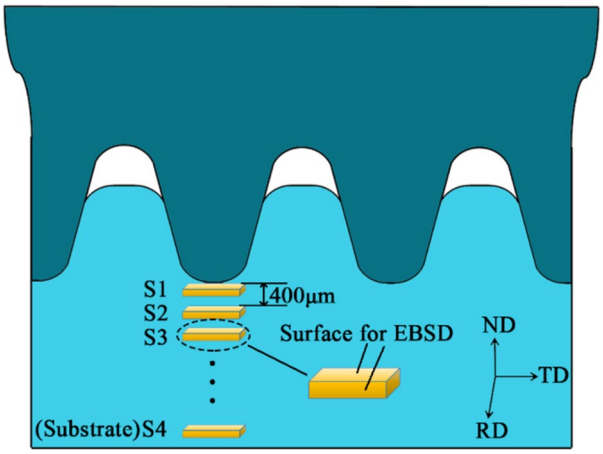

Figure 3. Sample processing and characterization for EBSD.

A/MPa	B/MPa	C	n	E/MPa
1118	510	0.0137	0.42	228,600

Table 2. Parameters of the Johnson–Cook model and Young's modulus of 40CrNi2MoV steel.

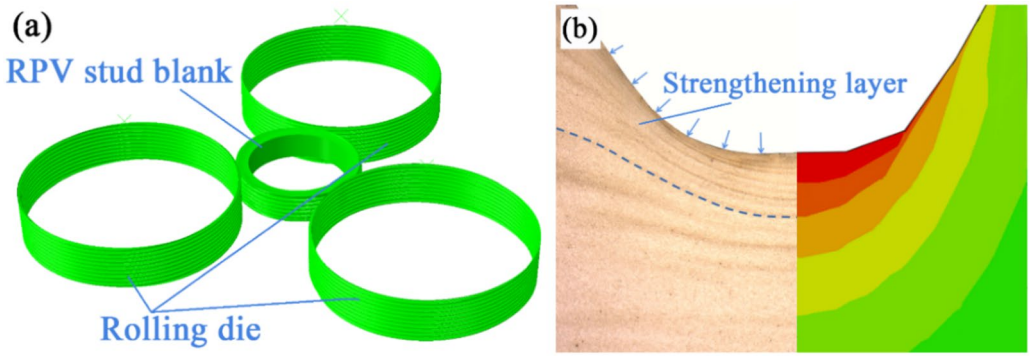

Figure 4. (**a**) Finite element model of the triaxial rolling process and (**b**) Metallographic and simulation comparison of thread sections.

of the thread. From the simulation results, it can also be seen that the stress in the thread root is getting smaller and smaller from the surface layer to the thread core. It indicates that the thread root was well strengthened during the thread rolling process, and the closer to the thread surface, the more obvious the strengthening effect.

Viscoplastic self-consistent model

The VPSC model works based on the shear mechanism of slip and twinning, and each grain is considered a viscoplastic ellipsoid embedded in an effective medium[28]. Input files for the VPSC model generally include the initial crystallographic texture, single crystal parameters, and boundary conditions. The initial texture file of the VPSC model consisted of nearly 5000 orientations obtained from the EBSD data of the matrix sample (EBSD data were taken every 10 points of the plot), and the single crystal parameters were mainly the elastic constants (Cij) of 40CrNi2MoV steel (calculated by Eq. (1)).

$$C_{ij} = \begin{pmatrix} 2.10e^{+05} & 1.85e^{+05} & 1.31e^{+05} & 0 & 0 & 0 \\ 1.85e^{+05} & 2.10e^{+05} & 1.31e^{+05} & 0 & 0 & 0 \\ 1.85e^{+05} & 1.31e^{+05} & 2.95e^{+05} & 0 & 0 & 0 \\ 0 & 0 & 0 & 6.0e^{+04} & 0 & 0 \\ 0 & 0 & 0 & 0 & 6.0e^{+04} & 0 \\ 0 & 0 & 0 & 0 & 0 & 1.2e^{+04} \end{pmatrix} \quad (1)$$

The stacking fault energies of BCC materials are generally very high, and their critical twinning stress does not vary much over a large temperature range of 4–300 K. Therefore, deformation twinning was negligible in the RPV stud material processed by triaxial rolling[29]. Moreover, the mechanical behavior of coarse-grained BCC materials is controlled by the slip of screw dislocations, which move only when the resolved shear stress is greater than the critical shear stress (CRSS), resulting in plastic deformation. The $\{110\}<111>$ and $\{112\}<111>$ slip systems are easily activated at room temperature[30], whereas the $\{123\}<111>$ slip system is only activated at elevated temperatures[31]. Therefore, the activated slip systems are set to $\{110\}<111>$, $\{112\}<111>$ in the file of the VPSC.

The Voce hardening model was used to describe the evolution of CRSS with cumulative shear strain within each grain.

$$\tau_c^s = \tau_0^s + \left(\tau_1^s + \theta_1^s \Gamma\right)\left(1 - \exp\left(-\Gamma\left|\frac{\theta_0^s}{\tau_1^s}\right|\right)\right) \quad (2)$$

where τ_c^s is the critical shear stress that causes slip during deformation, s is the whole deformation module, Γ is the accumulated shear within the grain, τ_0 is the initial CRSS, τ_1 is the steady-state critical decomposition shear stress, θ_0 is the initial hardening rate, θ_1 is the asymptotic hardening rate, and $\tau_0+\tau_1$ is the back-extrapolated CRSS of the deformation module 's'.

The parameters of Eq. (2) were obtained by fitting the stress–strain curve of the compression test shown in Fig. 5 (Table 3). It is noticeable from Fig. 5 that the compression test results fitted well with the VPSC fitting results.

In crystal plasticity theory, the analysis of deformation kinetics is crucial. The VPSC model works based on a rate-dependent plasticity theory, and its accuracy is closely related to the accuracy of the velocity gradient. The deformation in the grain is represented by the deformation gradient tensor F. The deformation gradient tensor $F = \frac{\partial x}{\partial X}$ can be expanded in the following form.

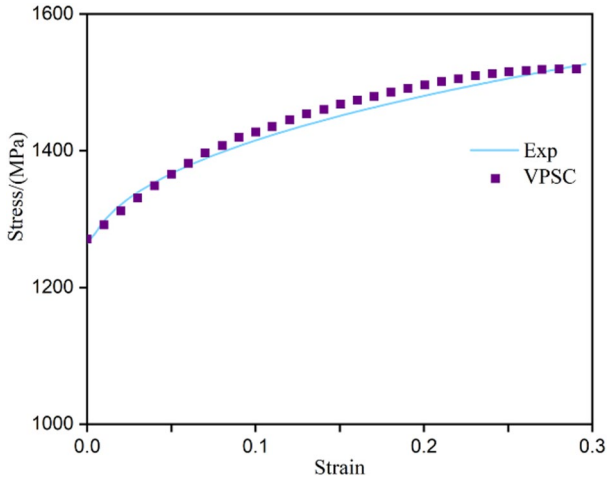

Figure 5. Comparison of the stress–strain curves obtained from the VPSC simulation and the experiment.

τ_0 (MPa)	τ_1 (MPa)	θ_0	θ_1
438	155	450	13

Table 3. Parameters of the Voce hardening model.

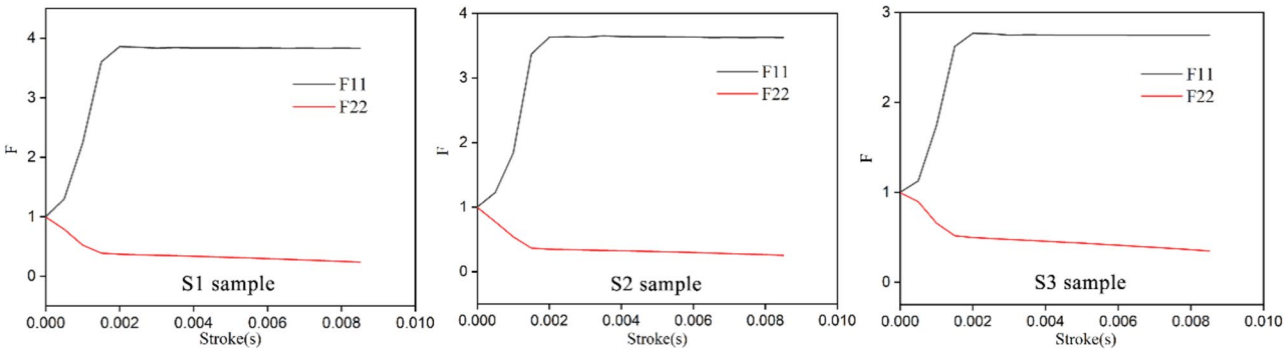

Figure 6. Deformation gradients of the S1, S2, and S3 samples.

$$F = \begin{pmatrix} \frac{\partial x_1}{\partial X_1} & \frac{\partial x_1}{\partial X_2} & \frac{\partial x_1}{\partial X_3} \\ \frac{\partial x_2}{\partial X_1} & \frac{\partial x_2}{\partial X_2} & \frac{\partial x_2}{\partial X_3} \\ \frac{\partial x_3}{\partial X_1} & \frac{\partial x_3}{\partial X_2} & \frac{\partial x_3}{\partial X_3} \end{pmatrix} \tag{3}$$

During the triaxial rolling process, the deformation of the external thread of the RPV stud occurred mainly due to axial tension and radial compression, Therefore, the tensile deformation gradient F11 along the axial direction of the threads, the compressive deformation gradient F22 along the radial direction of the threads were mainly derived. When the deformation gradient was greater than one, the material experienced tensile deformation, and when the deformation gradient was less than one, the material experienced compressive deformation. Defining the state variables in ABAQUS and associating them with the VUMAT subroutine to output the SDV state variable, the deformation gradient tensors F at different locations of the thread root were obtained. The deformation gradients on the root surface and subsurface (− 400 μm and − 800 μm) of the thread root are presented in Fig. 6. From S1 to S3, the final value of F11 gradually decreases while the value of F22 gradually increases, indicating that both the tensile deformation (along the axial direction) and compressive deformation (along the radial direction) of the material of the thread root decrease from S1 to S3.

The deformation gradient tensor F was converted into a velocity gradient tensor L according to Eq. (4) in Matlab with ΔT = 0.0005 S (FEM timestep) to predict the texture evolution at the thread root of the RPV stud during triaxial rolling.

$$\left[L^n\right] = \frac{\left[F^{n+1}\right] - \left[F^n\right]}{\left[F^{n+1}\right]} \times \frac{1}{\Delta T} \tag{4}$$

Installation and pretightening test

The installation method of RPV studs is different from the general installation method of high-strength bolts. In the present study, instead of the torque or nut corner methods, residual elongation was used to preload the stud. The stud was first installed on the simulated installation test platform and then stretched by a hydraulic tensioner, as shown in Fig. 7a. When the stud stretching force reached the design value, the displacement of the measuring rod in the stud was calculated by a dial indicator. Subsequently, the nut was tightened, and the oil pressure in the hydraulic tensioner was removed. The residual displacement of the measuring rod was measured.

At the same time, to test the RPV studs for jamming problems, the installation was carried out with different eccentricity distances shown in Fig. 7b. Rotational torques and bolt positions were recorded in real-time every six mm during the test.

Results and discussion

Dynamic recrystallization

Continuous dynamic recrystallization (CDRX) occurred during triaxial rolling due to the severe plastic deformation of the material. Subgrain boundaries generated under low strains were gradually transformed into ultrafine grains with high-angle grain boundaries under high strains. The inverse pole figures of RD–TD plane of the S1–S4 samples are displayed in Fig. 8a–d, respectively (high-angle grain boundaries (HAGBs; > 15°) and low-angle grain boundaries (LAGBs; < 15°) are represented by the black and green solid lines, respectively). The deformation of the material gradually decreased from S1 to S4, and dislocations within the grain decreased; therefore, LAGBs formed within the grain also gradually decreased. Moreover, ultra-fine grains transformed by LAGBs gradually decreased, and ultra-fine grains in the S1–S3 samples (– 400 μm) were distributed around coarse grains with HAGBs[32]. In contrast, very few ultra-fine grains existed in the S4 specimen.

The recrystallization diagrams of the S1–S4 samples are exhibited in Fig. 8e–h, respectively. The S1–S3 specimens were subjected to the radial and tangential forces of the rolling dies and underwent CDRX. LAGBs were converted into subgrains, which then formed ultra-fine grains with HAGBs by recrystallization. Therefore, a large number of deformed and fully recrystallized grains were present in the S1–S3 samples. The S4 specimen was dominated by substructured grains after forging and heat treatments (quenching and tempering). The linear distributions of S1–S4 misorientations were calculated along L1, L2, L3, and L4 (line between two coarse grains), respectively, using the Misorientation profile in Channel 5. It is noticeable from Fig. 9 that the S4 specimen was dominated by high-angle coarse crystals. The number of HAGBs in the S1–S3 samples gradually decreased, and also the average orientation angle gradually decreased; thus, the orientation of initial grains on the outer surface of the RPV stud evolved significantly after triaxial rolling. The closer to the surface of the external thread root, the finer the grain size and the higher the number of grain boundaries. It can also be observed through the Scanning electron microscope images that after forging and heat treatment, the microstructure of the thread root (S4) was tempered sorbite, and after the triaxial rolling process, the grain size of the S1 sample in the surface layer of the

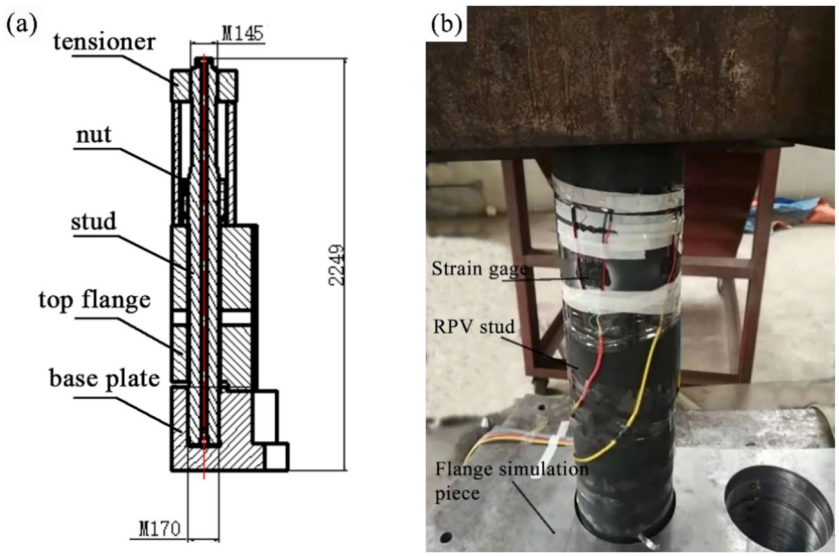

Figure 7. (**a**) Tensile pre-tightening of the RPV stud and (**b**) Installation.

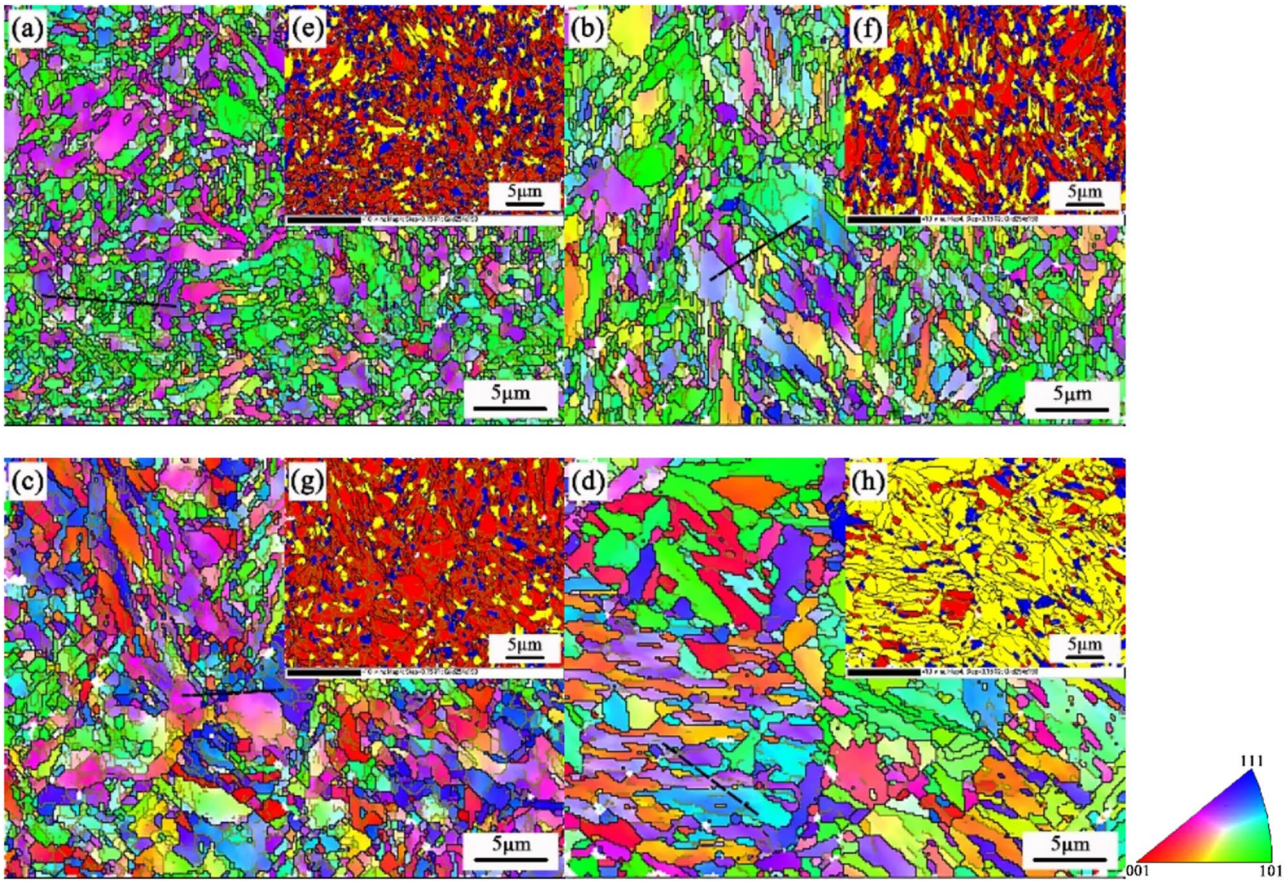

Figure 8. Inverse pole figures of S1–S4 samples (**a**–**d**) and Recrystallization diagrams of the S1–S4 samples (**e**–**h**).

thread root was significantly reduced compared to the grain size in the substrate S4 sample, as shown in Fig. 10. Hence, the strength of the external threads was effectively improved[33].

Texture analysis

During the triaxial rolling process, textures were formed in the external threads of the RPV stud, especially in the thread root area that was severely compressed and sheared. The finite element model was coupled with the VPSC model to predict textures at different depths along the radial direction of the external thread root of the RPV stud, and the results were verified with the EBSD data. Using the orientation distribution function (ODF) in the Euler space, the main textures of the ND-TD section of the S1–S3 specimens with surface and subsurface layers at $\varphi 2 = 45°$ were analyzed[34]. The algorithm used for ODFs calculations was spherical harmonics, with the half-width set to 5° and the cell width set to 5°. It is noticeable from Fig. 12 that the polar coordinate values of the simulated texture values were basically consistent with those of the experimental texture; however, some deviations still existed between them because the interaction between grains and the generation of dislocation substructures were not considered during VPSC simulations[35,36]. The distribution of texture intensity in simulations was basically consistent with the experiments. But there were some differences in the values of texture intensity. The maximum texture intensity of S1 and S2 samples in the experiment were 9.13 and 8.35, respectively, while the predicted values of VPSC were 10.06 and 8.11, respectively. The reason for this is the limited orientations considered input and the choice of sampling for input orientations[24]. Compared with the typical texture diagram of body-centered cubic metal materials (Fig. 11), it is found that the texture strength was significantly enhanced under the synergistic action of radial pressure and tangential shear force after triaxial rolling. As shown in Fig. 12, obvious rolling textures were formed in the S1 and S2 samples. The main texture of the S1 specimen was copper{112}<111>; however, it also contained an α{001} <110> texture and a γ{111} <110> texture. In the S2 sample, the main texture was γ{111} <110>, whereas in the S3 sample, a weak γ{111} <110> texture was formed.

Figure 13 displays the strength variations of the α, γ, and ε textures of the S1–S3 specimens during triaxial rolling. The S1 sample was subjected to frictional force along the RD direction and compression force along the ND direction by the rolling dies, and its grains became stretched along the RD direction and compressed along the ND direction, generating an α{001}<110> texture. At the same time, since the S1 sample was subjected to a stronger shear force compared to the S2 and S3 samples, it was easier to cause the rotation of the exactly oriented cube grains, which promotes the formation of the copper texture in the S1 sample[37]. The S2 and S3 samples were located in the subsurface layer of the thread root and were subjected to radial rolling force; therefore, a rolling texture was formed in them due to strain deformation. During the triaxial rolling process, as strain accumulated,

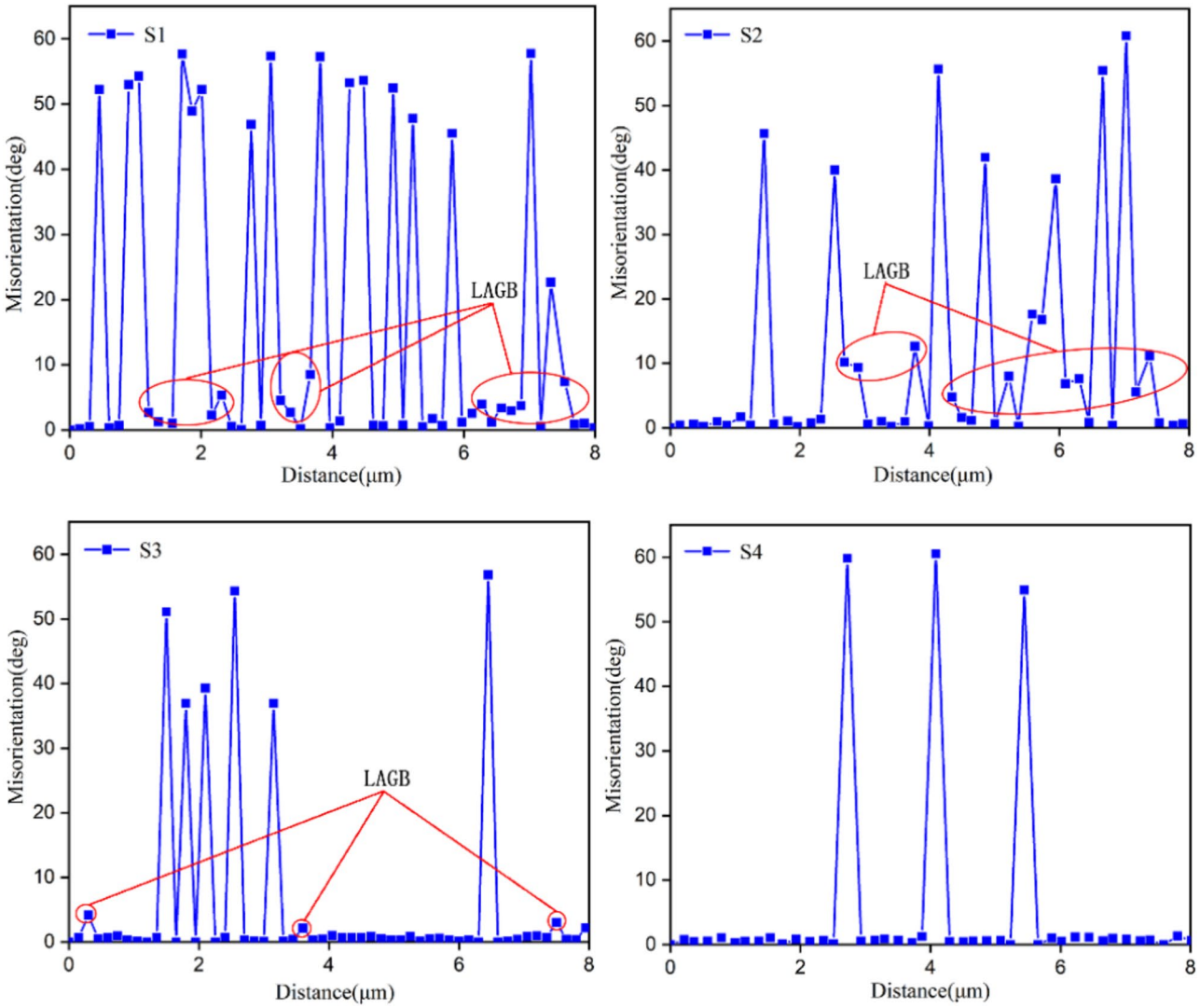

Figure 9. EBSD-grain boundary images of the S1–S4 samples.

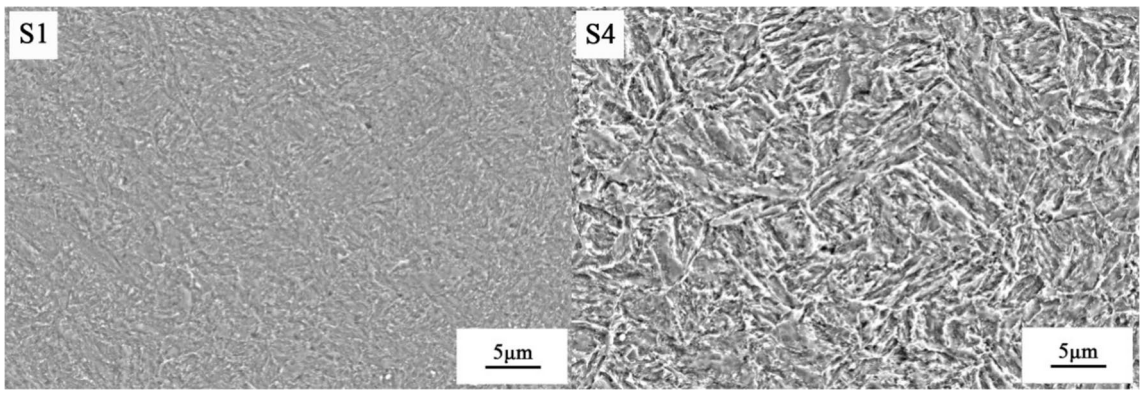

Figure 10. Scanning electron microscope images of the S1, S4 samples.

the dislocation density inside the grains at the thread root gradually increased, which resulted in CDRX. As the {111} surface is the closely packed plane of cubic crystal structures with low surface energy, the recrystallization process generated textures based on the {111} surface. The rotational motion and radial feed movement of the rolling die elongated the grains at the thread root along the axial direction of the RPV stud; thus, a strong texture along the < 110 > or < 112 > orientation was formed.

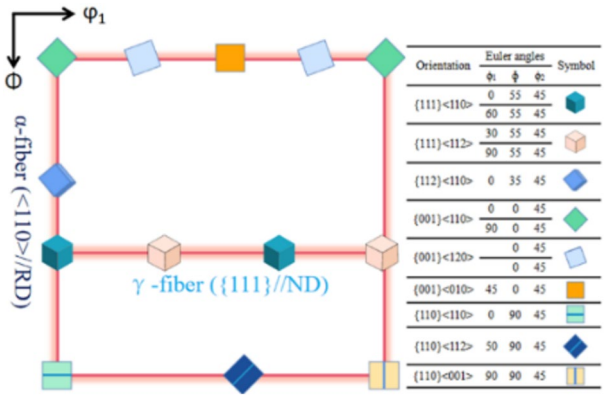

Figure 11. Typical textures of body-centered cubic crystals.

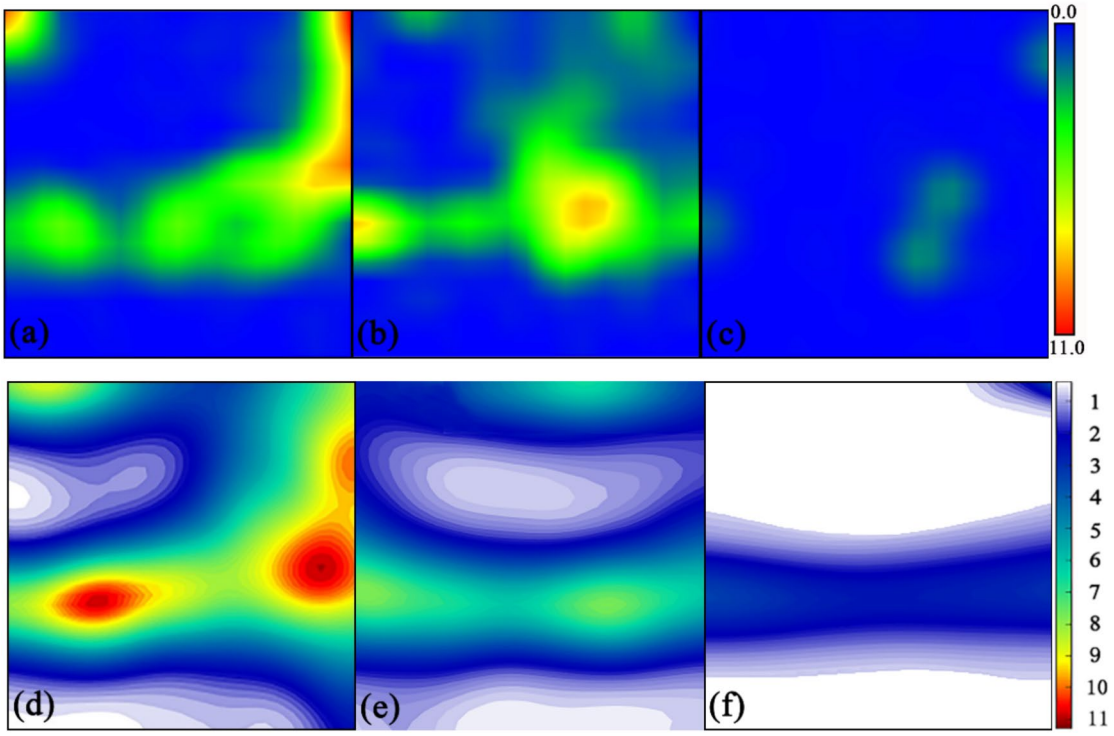

Figure 12. Comparison of experimental and simulated textures: (**a**–**c**) experimental textures of the S1–S3; (**d**–**f**) simulated textures of the S1–S3.

Installation and pre-tightening test

The RPV stud installation and pre-tightening test analyzed the stability and reliability of the stud. In the pre-tightening test, when the high-pressure cylinder was filled with oil and pressurized, the internal piston of the cylinder moved upward and drove the main nut upward. The main nut was locked at the tension holding point, and the residual elongation of the RPV stud was checked after the pressure was released from the high-pressure cylinder. The residual elongations of the RPV stud processed by rolling and turning under different loading pressures are presented in Fig. 14. When the loading pressure reached 110 MPa, the residual elongations of the rolled and turned parts of the RPV stud were 1.759 mm and 1.881 mm, respectively. Hence, under the same loading pressure, the residual elongation of rolled parts was reduced by 6%. During triaxial rolling, grains at the external thread root of the RPV stud were subjected to severe plastic deformation, resulting in a reduction in grain size, an increase in dislocations, and a strong texture. This grain structure facilitates the improvement of tensile properties and reduces the deformation of the material when subjected to tensile loads. At the same time, the rolling process forms a hardened layer on the thread surface and introduces residual compressive stresses, which also reduce the residual elongation of the RPV stud.

The variations of installation torque with displacement in the turned and rolled parts of the RPV stud at different eccentric distances (0.0, 0.3, and 0.5 mm) in the installation test are exhibited in Fig. 15. The installation

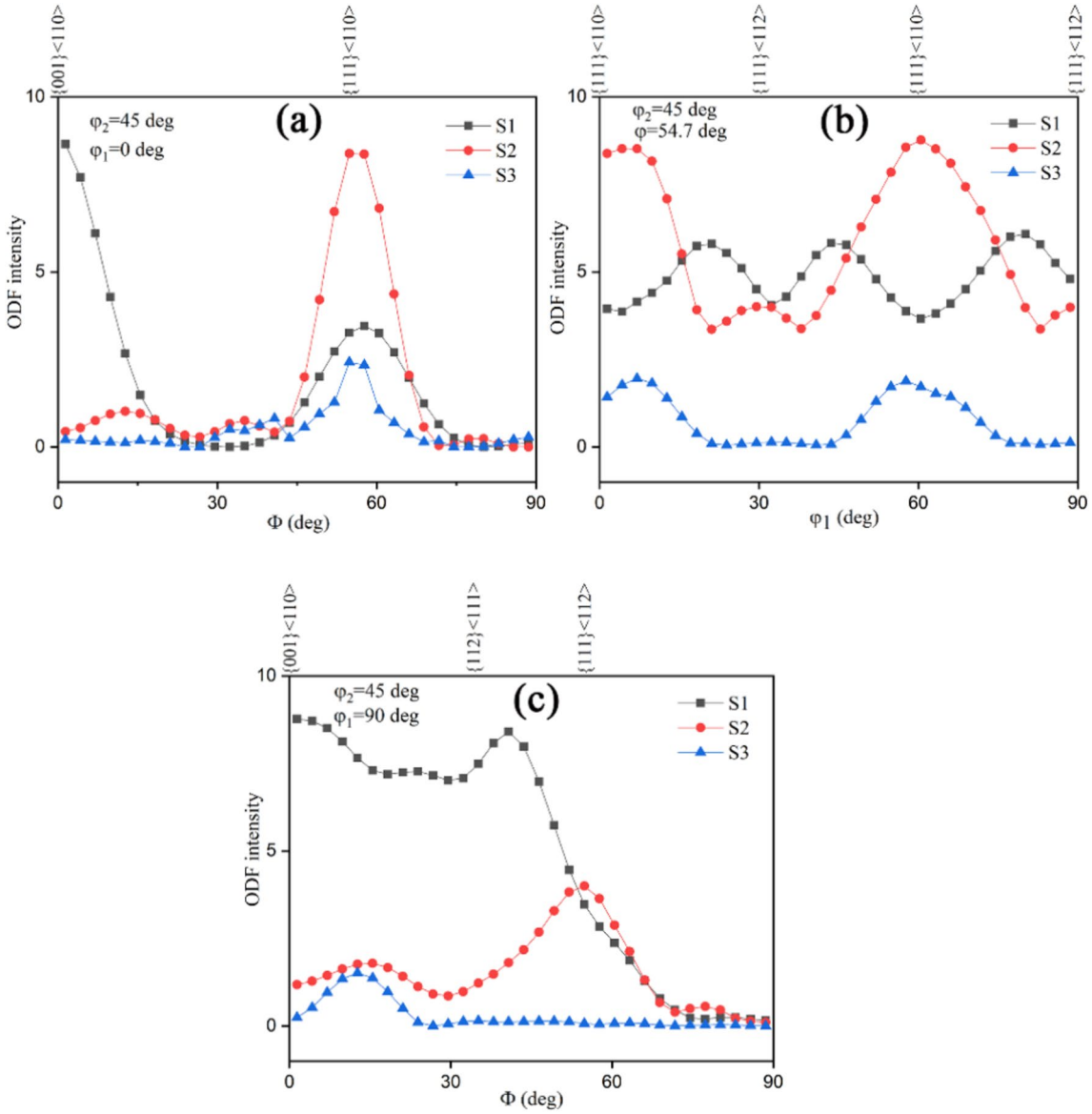

Figure 13. Orientation intensity plots of the S1-S3 samples: (**a**) α texture; (**b**) γ texture; (**c**) ε texture.

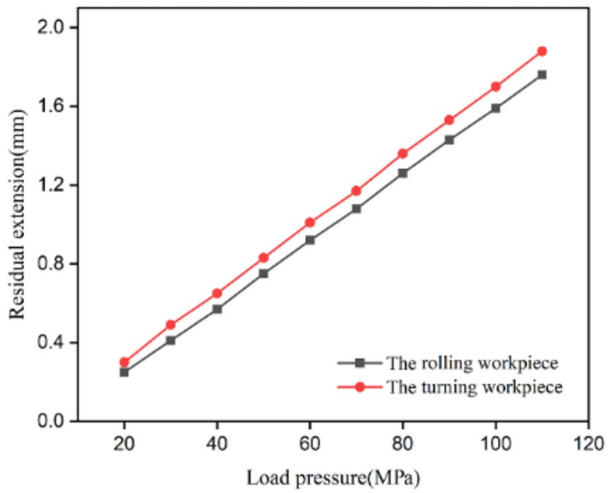

Figure 14. Residual elongations of the rolled and turned parts of the RPV stud during the pretightening test.

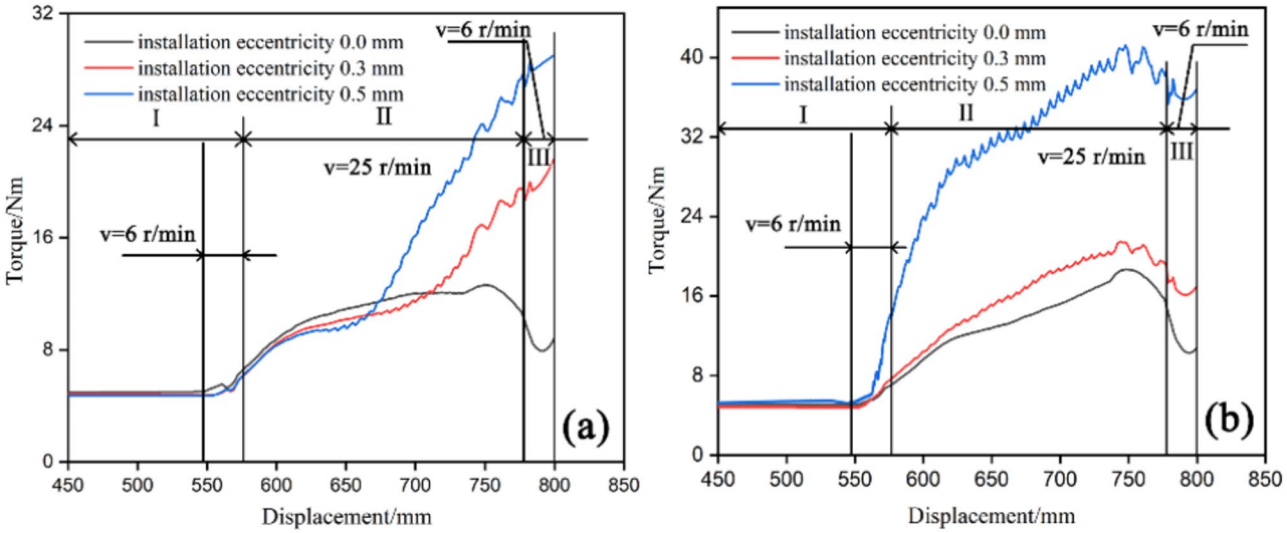

Figure 15. Installation torques at different eccentricities: (**a**) Turned part and (**b**) Rolled part.

process was divided into three stages: (I) RPV stud feeding to the first four threads between 450 and 572 mm at 6 r/min. (II) Fast screwing process between 572 and 776 mm at 25 r/min, and (III) Speed-down process between 776 and 800 mm at 6 r/min.

In stage I, between 450 and 548 mm, the RPV stud was not yet in contact with the simulated flange, and the torque was constant. The stud contacted the first four threads of the simulated flange between 548 and 572 mm, and the torque started to increase.

In stage II, the installation torque of both turned and rolled parts increased with the number of thread engagements. The torque of the turned part in the initial stage decreased as the eccentricity increased, indicating that the verticality of the RPV stud during turning was not good enough (Fig. 15a). The installation torque of the rolled part was larger than that of the turned part in stage II because the external threads had better surface quality and strength, thereby being able to withstand greater torques. The machining size of the rolled part was more stringent than that of the turned part, the fit clearance between the rolled part and the main nut was smaller, and the torque during installation was larger, causing better stability of the RPV stud.

As the rolling process mirrored the threads of the rolling die on the RPV stud, in stage III, the geometric accuracy of the threads was higher, the strength of the rolled part was higher, and the yield ratio was greater, resulting in less deformation during installation and a more stable fit clearance between the simulated flange bore threads and the stud. Hence, the installation torque of the rolled part was also more stable than that of the turned part. As the installation speed decreased from 25 to 6 r/min, the installation torque of the rolled parts at different eccentricities also decreased (Fig. 15b). However, a significant cumulative error occurred in the threads of the turned part, resulting in poor geometric accuracy and low stud strength. The RPV stud might be skewed or deformed during screwing in, resulting in increased friction between the stud and the simulated flange bore threads. Therefore, as the installation speed decreased, the installation torque of the turned part at eccentricities of 0.3 mm and 0.5 mm tended to rise and even exceeded the design limit.

Conclusion

Here an RPV stud was prepared by triaxial rolling, the microstructure evolution, installation, and preload performance of which were investigated. The main observations of this study were as follows.

During triaxial rolling, the RPV stud was subjected to the radial, axial, and tangential forces of the rolling dies, resulting in severe plastic deformation, which caused the continuous dynamic recrystallization of the surface and subsurface grains of the external threads. Subsequently, low-angle grain boundaries were transformed into sub-grains, and ultra-fine grains separated by high-angle grain boundaries were formed by recrystallization; thus, the grain size at the thread root was refined.

The finite element model was coupled with VPSC simulations to predict texture distribution and evolution in the rolling strengthening process of the RPV stud, and the results were verified by EBSD experiments. The S1 sample was subjected to frictional force along the RD direction and compression force along the ND direction; thus, its grains got stretched along the RD direction and compressed along the ND direction, resulting in an $\alpha\{001\}<110>$ texture. Under the combined action of shear force and ultra-fine grains, the S1 sample also had a strong copper texture. The S2 and S3 samples were mainly subjected to radial rolling force; hence, their main textures were $\{111\}<110>$ and $\{111\}<112>$.

In the installation tests with different eccentric distances, the rolled part of the RPV stud had a more stable installation torque than the turning part. Due to the thread accumulation error and the deformation of the external threads of the turned part, when the eccentricities were 0.3 mm and 0.5 mm, the torque of the turned part increased linearly as the number of engaged threads increased; meanwhile, the torque of the rolled part was within a stable range due to its higher strength, better accuracy, and good surface quality.

Data availability

The datasets used and/or analysed during the current study available from the corresponding author on reasonable request.

Received: 17 April 2024; Accepted: 23 July 2024
Published online: 06 September 2024

References

1. Huang, T., Jin, L., Chen, T. & Qiu, Z. Development and evaluation of welding repair for threaded hole of reactor pressure vessel flange. *Int. J. Press. Vessels Piping* **191**, 104341 (2021).
2. Choi, J. B., Kim, J. S., Kim, Y. J., Choi, S. N. & Jang, K. S. Evaluation of the crack tip stress distribution considering constraint effects in pressure vessel. *Am. Soc. Mech. Eng. Press. Vessels Piping Div. Publ. PVP* **388**, 183–188 (1999).
3. Maciel, D. T., Filho, S. L. M. R., Lauro, C. H. & Brandão, L. C. Characteristics of machined and formed external threads in titanium alloy. *Int. J. Adv. Manuf. Technol.* **79**(5–8), 779–792 (2015).
4. Shao, Y., Peng, W., Yu, X., Oleksandr, M. & Titov, V. Effect of rolling parameters on forming quality of flat cross wedge rolling thread shafts. *Proc. Inst. Mech. Eng. Part E J. Process Mech. Eng.* **235**(2), 230–237 (2020).
5. Zhang, S., Fan, S., Zhang, P., Zhu, Q. & Zhao, S. The formation mechanism of protrusion of long thread by axial self-infeed rolling process. *Proc. Inst. Mech. Eng. Part B J. Eng. Manuf.* **234**(10), 1302–1310 (2020).
6. Liu, Z. Q., Song, J. L., Li, Y. T., Li, X. D. & Wang, M. F. Process and properties on the precision forming of spline cold rolling. *Adv. Mater. Res.* **154–155**, 191–196 (2010).
7. Dawei, Z., & Shengdun, Z. Research development of cold rolling precision forming process of external thread. *China Metal Form. Equip. Manuf. Technol.* (2015).
8. Zhang, S., Zhang, D., Jiang, H., Jiang, F. & Zhao, S. Numerical and experimental analysis of deformation behaviors and microstructure evolution in the thread rolling process. *J. Market. Res.* **19**, 230–242 (2022).
9. Zhang, S., Zhang, D., Zhao, S., Jiang, F. & Lee, M.-G. Characteristics of surface and subsurface of formed thread parts by axial-infeed thread rolling process. *Chin. J. Aeronaut.* **36**(3), 471–481 (2023).
10. Mohandesi, A., Rafiee, M.A., Maffi, O. & Saffarzadeh, P. Dependence of the yield and fatigue strength of the thread rolled mild steel on dislocation density. *J. Manuf. Sci. Eng.* **129**(1), 216–222 (2007).
11. Zhu, W. *et al.* Evolution of surface morphology and microstructure in reactor pressure vessel studs during triaxial rolling. *Int. J. Adv. Manuf. Technol.* **126**(9–10), 4591–4605 (2023).
12. Kao, Y.-C., Cheng, H.-Y. & She, C.-H. Development of an integrated CAD/CAE/CAM system on taper-tipped thread-rolling die-plates. *J. Mater. Process. Technol.* **177**(1–3), 98–103 (2006).
13. Nitu, E., Tabacu, S., Iordache, M. & Iacomi, D. Finite element analysis and experimental validation of the wedge rolling process. *Proc. Inst. Mech. Eng. Part B J. Eng. Manuf.* **227**(9), 1325–1339 (2013).
14. Zhang, D.-W., Zhang, C., Tian, C. & Zhao, S.-D. Forming characteristic of thread cold rolling process with round dies. *Int. J. Adv. Manuf. Technol.* **120**(3–4), 2503–2515 (2022).
15. Liu Lei, L. P. Present situation and development tendency of high strength bolt steel. *J. Shanghai Univ. Eng. Sci.* **24**(02), 173–179 (2010) (**(in Chinese)**).
16. Li YaFei, W. Y. & JiaJu, Li. Heat treatment techniques for studs used on pressure vessel of nuclear reactor. *CFHI Technol.* **1**, 28–31 (2021) (**(in Chinese)**).
17. Zhou, W. *et al.* Design of intelligent processing system for stud pretensioning data of reactor pressure vessel. *China Nuclear Power* **10**(01), 28–33 (2017) (**(in Chinese)**).
18. Lebensohn, R. A. & Tomé, C. N. A self-consistent anisotropic approach for the simulation of plastic deformation and texture development of polycrystals: Application to zirconium alloys. *Acta Metall. Mater.* **41**(9), 2611–2624 (1993).
19. Nabi, B. *et al.* Origin of the {111}⟨112⟩ cold rolling texture development in a soft magnetic Fe-27%Co alloy. *J. Mater. Eng. Perform.* **28**(6), 3767–3776 (2019).
20. Bal, B. A Study of different microstructural effects on the strain hardening behavior of hadfield steel. *Int. J. Steel Struct.* **18**(1), 13–23 (2018).
21. Després, A. *et al.* Contribution of intragranular misorientations to the cold rolling textures of ferritic stainless steels. *Acta Mater.* **182**, 184–196 (2020).
22. Takajo, S., Vogel, S. C. & Tomé, C. N. Viscoplastic self-consistent polycrystal modeling of texture evolution of ultra-low carbon steel during cold rolling. *Modell. Simulat. Mater. Sci. Eng.* **27**(4), 045003 (2019).
23. Chen, S. F., Song, H. W., Zhang, S. H., Cheng, M. & Lee, M. G. Effect of shear deformation on plasticity, recrystallization mechanism and texture evolution of Mg–3Al–1Zn alloy sheet: Experiment and coupled finite element-VPSC simulation. *J. Alloy. Compd.* **805**, 138–152 (2019).
24. Mishin, V. V., Shishov, I. A., Stolyarov, O. N., Kasatkin, I. A. & Glukhov, P. A. Effect of cold rolling route on deformation mechanism and texture evolution of thin beryllium foils: Experiment and VPSC simulation. *Mater. Charact.* **164**, 110350 (2020).
25. Saleh, A. A., Haase, C., Pereloma, E. V., Molodov, D. A. & Gazder, A. A. On the evolution and modelling of brass-type texture in cold-rolled twinning-induced plasticity steel. *Acta Mater.* **70**, 259–271 (2014).
26. Buchely, M. F. *et al.* Experimental development of Johnson-Cook strength model for different carbon steel grades and application for single-pass hot rolling. *Steel Res.Int.* **91**(7), 1900670 (2020).
27. Zhang, D.-W., Cui, M.-C., Cao, M., Ben, N.-Y. & Zhao, S.-D. Determination of friction conditions in cold-rolling process of shaft part by using incremental ring compression test. *Int. J. Adv. Manuf. Technol.* **91**(9–12), 3823–3831 (2017).
28. Kang, G. P., Lee, K., Kim, Y. H., Park, S. J. & Shin, K. S. Implementation of VPSC polycrystal model into rigid plastic finite element method and its application to Erichsen test of Mg alloy. *Met. Mater. Int.* **23**(5), 930–939 (2017).
29. Shi, S., Zhu, L., Zhang, H., Sun, Z. & Ahuja, R. Mapping the relationship among composition, stacking fault energy and ductility in Nb alloys: A first-principles study. *Acta Mater.* **144**, 853–861 (2018).
30. Du, C., Maresca, F., Geers, M. G. D. & Hoefnagels, J. P. M. Ferrite slip system activation investigated by uniaxial micro-tensile tests and simulations. *Acta Mater.* **146**, 314–327 (2018).
31. Fischer, T., Dahlberg, C. F. O. & Hedström, P. Sensitivity of local cyclic deformation in lath martensite to flow rule and slip system in crystal plasticity. *Comput. Mater. Sci.* **222**, 112106 (2023).
32. Hamad, K., Megantoro, R. B. & Ko, Y. G. Microstructure and texture evolution in low carbon steel deformed by differential speed rolling (DSR) method. *J. Mater. Sci.* **49**(19), 6608–6619 (2014).
33. Hansen, N. Hall-Petch relation and boundary strengthening. *Scripta Materialia.* **51**(8), 801–806 (2004).
34. Ren, C. X., Wang, Q., Hou, J. P., Zhang, Z. J. & Zhang, Z. F. Effect of work-hardening capacity on the gradient layer properties of metallic materials processed by surface spinning strengthening. *Mater. Charact.* **177**, 11179 (2021).
35. Brown, D. W. *et al.* Development of crystallographic texture during high rate deformation of rolled and hot-pressed beryllium. *Metall. Mater. Trans. A* **36**(4), 929–939 (2005).

36. Patra, A. & Tomé, C. N. A dislocation density-based crystal plasticity constitutive model: Comparison of VPSC effective medium predictions with ρ-CP finite element predictions. *Modell. Simulat. Mater. Sci. Eng.* **32**(4), 045014 (2024).
37. Jiang, W., Wu, X., Yang, P. & Gu, X. Relationship between the initial 100 textures and the shear textures developed in sheet surface during hot rolling of non-oriented silicon steel. *Mater. Charact.* **182**, 111534 (2021).

Acknowledgements
The authors would like to express their gratitude to the "Research on General International Standards of Equipment Manufacturing Foundation" (2021YFF0601702) for the financial support.

Author contributions
W.Z.: Investigation, Methodology, Writing–Original draft preparation; H.L., P.C. and F.F.: Experiment preparation; D.W. and L.L: Writing–Reviewing and Editing; P.Z.: Methodology; Revision.

Funding
This research was supported by Research on General International Standards of Equipment Manufacturing Foundation, (Grant No. 2021YFF0601702).

Competing interests
The authors declare no competing interests.

Additional information
Correspondence and requests for materials should be addressed to D.W.

Reprints and permissions information is available at www.nature.com/reprints.

Publisher's note Springer Nature remains neutral with regard to jurisdictional claims in published maps and institutional affiliations.